Power System Protection and Control
ISSN:1674-3415

AN INTELLIGENT DECISION SUPPORT FRAMEWORK FOR FLOOD FORECASTING AND STRUCTURAL SAFETY MONITORING IN HYDROPOWER SYSTEMS: INTEGRATION WITH POWER SYSTEM PROTECTION AND CONTROL

Soraya Sarwari[1], Yan Qiao[2],*, Monir Ahmad Meahrayen[3], Prasanna Koirala[4], Gu Yihang[5]

[1] College of Hydraulic & Environmental Engineering, China Three Gorges University, Yichang, Hubei, P.R. China, sarwarisoraya24@gmail.com
[2] College of Hydraulic & Environmental Engineering, China Three Gorges University, Yichang, Hubei, P.R. China, monir.meahrayen94@gmail.com
[3] College of Hydraulic & Environmental Engineering, China Three Gorges University, Yichang, Hubei, P.R. China, prasannakoirala1555@gmail.com
[4] Pokhara University / Tamor Energy P. Ltd, Kupondole Road, Lalitpur, Nepal
[5] College of Hydraulic & Environmental Engineering, China Three Gorges University, Yichang, Hubei, P.R. China, 823760787@qq.com
***Corresponding author:** Yan Qiao (yanqiao666@163.com)

Received: 15/05/2026 **Revised**: 12/06/2026 **Accepted**: 01/07/2026

***ABSTRACT*:**

Most hydropower stations still run flood forecasting and dam safety monitoring as two separate operations, with no shared decision logic between them — even though a hydrological risk can become a structural risk within hours. This paper proposes a four-layer protection and control framework — Data Acquisition, Hydrological Forecasting, Structural Risk Assessment, and Application/Control — that couples hydrological forecast uncertainty with physical dam integrity in a single SCADA-interfaced decision pipeline.

A calibrated HBV (Hydrologiska Byråns Vattenbalansavdelning) rainfall-runoff model is coupled with an LSTM network for residual error correction, producing 6–72 hour streamflow forecasts. A Fuzzy-Bayesian engine then maps these forecasts together with concurrent structural signals — seepage, deformation, and reservoir level — onto a four-tier risk scheme consistent with SL 314-2018, with risk-level triggers passed to SCADA/EMS platforms over IEC 61850.

Applied to the Kunhar River Basin in Pakistan, the HBV-LSTM model reaches NSE = 0.91 and RMSE = 14.8 m^3/s, a 16.7-percentage-point NSE gain over standalone HBV, with peak-flow error falling from 14.1% to 7.2%. Under the RCP8.5 scenario, the 100-year design flood rises from 6,240 to 8,150 m^3/s, pushing the baseline risk classification from Level II to Level III in 38% of ensemble members. The 6–12 hour forecast horizon enables advance generation dispatch, cutting spillage losses by 5%–8%, while Level IV emergency commands execute within 100 ms via GOOSE messaging.

The framework offers a standards-compliant pathway for coordinating hydropower flood response with power-system protection, and the modular four-layer design should transfer to other climate-sensitive basins without requiring a full SCADA rebuild.

Keywords*: Hydropower Decision-Making; Hydrological Forecasting; Hbv Model; Lstm; Dam Safety Monitoring; Fuzzy-Bayesian Risk Assessment; Iec 61850; Scada/Ems Integration..*

INTRODUCTION

Hydropower supplies roughly 16% of global electricity and over 70% of renewable generation capacity (International Energy Agency [IEA], 2023). Climate change is steadily eroding the assumptions that much of this infrastructure was designed under. In basins with strong orographic precipitation — the upper Indus tributaries in Pakistan, the Yangtze headwaters, Himalayan-fed systems generally — peak discharge is projected to rise 20%–45% under high-emission scenarios by mid-century (Immerzeel et al., 2020; Lutz et al., 2016; Döll et al., 2023;

Turner et al., 2019). That intensification rarely stays confined to the hydrological record alone. The World Bank (2022) estimates unplanned spillage and curtailment already cost operators USD 1.2–3.8 billion annually across South and Southeast Asia, and ICOLD (2022) traces more than a third of 172 documented dam failures between 1959 and 2021 back to flood-routing decisions made without adequate awareness of concurrent structural anomalies. Read together, these figures point less to a forecasting problem or a monitoring problem in isolation than to a coordination problem — one with direct consequences for power system protection and control.

Both halves of that coordination problem have, on their own, received considerable attention. On the forecasting side, ensemble numerical weather prediction coupled with distributed rainfall-runoff models has pushed useful lead times beyond 72 hours (Cloke & Pappenberger, 2009; Pappenberger et al., 2015). The HBV model (Bergström, 1992) remains a workhorse for mountainous, snowmelt-influenced catchments (Seibert & Vis, 2012; Zhang et al., 2013), and LSTM networks (Hochreiter & Schmidhuber, 1997) have proven effective at correcting its systematic biases, with reported NSE values of 0.85–0.94 across diverse catchments (Kratzert et al., 2018; Gauch et al., 2021; Frame et al., 2022). On the structural side, distributed sensor networks feed into Bayesian and fuzzy-logic risk schemes that handle the linguistic uncertainty involved in translating raw sensor readings into operational decisions (Altarejos-García et al., 2012; Hariri-Ardebili & Pourkamali-Anaraki, 2018; Fenton & Neil, 2018). What remains comparatively rare is a framework that routes both streams through one decision pipeline wired into grid control infrastructure, rather than two parallel dashboards that operators must reconcile manually (Xu et al., 2023; Li et al., 2024).

Three gaps follow from this. First, existing hydropower management systems typically run forecasting and structural monitoring on separate platforms with no automatic cross-domain risk aggregation, so compound flood-structural events tend to produce delayed or incoherent responses. Second, the translation of risk classification into dispatch and protection actions lacks standardized protocols at most facilities, leaving operators to rely on judgment rather than algorithmic guidance under time pressure. Third, published frameworks that do attempt this integration are rarely validated against observed data in climate-sensitive mountainous basins, precisely where hydrological and structural risk tend to rise together rather than independently.

This paper addresses these gaps directly. We (1) couple HBV and LSTM within a hybrid forecasting pipeline calibrated for a high-elevation headwater catchment; (2) build a Fuzzy-Bayesian risk engine that aggregates hydrological and structural signals in one step, with membership functions and indicator weights reported explicitly and tested for sensitivity; (3) interface the resulting four-tier risk scheme with SCADA/EMS via IEC 61850, specifying logical-node mappings and GOOSE latency targets at an implementation level; and (4) validate the full chain retrospectively on the Kunhar River Basin, Pakistan, under RCP4.5/RCP8.5 projections to 2050. We treat this as a first validation step rather than a finished operational system — the remaining gap to field deployment is discussed candidly in Section 5.2. Section 2 describes the study area and data; Section 3 presents the methods; Sections 4 and 5 cover results and discussion; Section 6 concludes.

STUDY AREA AND DATA

The Kunhar River Basin, located in the Khyber Pakhtunkhwa province of northern Pakistan (34.2°N–034.9°N, 73.4°E–74.1°E), was selected as the case study site. The basin drains an area of approximately 2,527 km² from the high-elevation ridgelines of the western Himalayas to the Tarbela Reservoir inflow zone. Elevations range from 640 m at the outlet to 5,290 m at the basin divide, producing marked altitudinal precipitation gradients and a seasonally complex runoff regime dominated by monsoon rainfall (July–September) and snowmelt (April–June). The Kunhar Basin is representative of a broader class of hydropower catchments across South and Central Asia facing intensifying hydrological extremes under climate change (Lutz et al., 2016; Immerzeel et al., 2020), which makes it a reasonable test case for the proposed framework.

The Balakot hydrological station (gauge ID PK-BLK-03), located at the basin outlet, serves as the primary calibration and validation reference. Daily discharge records spanning 1990–2018 were obtained from the Surface Water Hydrology Project of the Pakistan Meteorological Department (PMD). Meteorological forcing data — daily precipitation, maximum and minimum temperature, and relative humidity — were compiled from six PMD stations distributed across elevation bands and supplemented with bias-corrected ERA5 reanalysis for the same period (Hersbach et al., 2020). Spatial inputs include a 30 m resolution SRTM digital elevation model and a land-use/land-cover classification derived from Landsat-8 imagery. Climate scenario data for RCP4.5 and RCP8.5

DOI: 10.46121/pspc.54.3.13

(2019–2050) were obtained from the CORDEX-SA multi-model ensemble, following the delta-change bias-correction approach of Teutschbein and Seibert (2012).

Structural monitoring inputs — reservoir level gauges, piezometers, and displacement transducers — were synthesized from design specification ranges consistent with SL 314-2018 and ICOLD Bulletin 158 (2013), rather than drawn from a long-term instrumented record. We are explicit about this throughout the paper: the synthesized series let us test whether the Fuzzy-Bayesian engine behaves sensibly across the full range of plausible structural states, but they are a stand-in for field data, not a replacement for it. Section 5.2 returns to what this limitation does and does not allow us to claim.

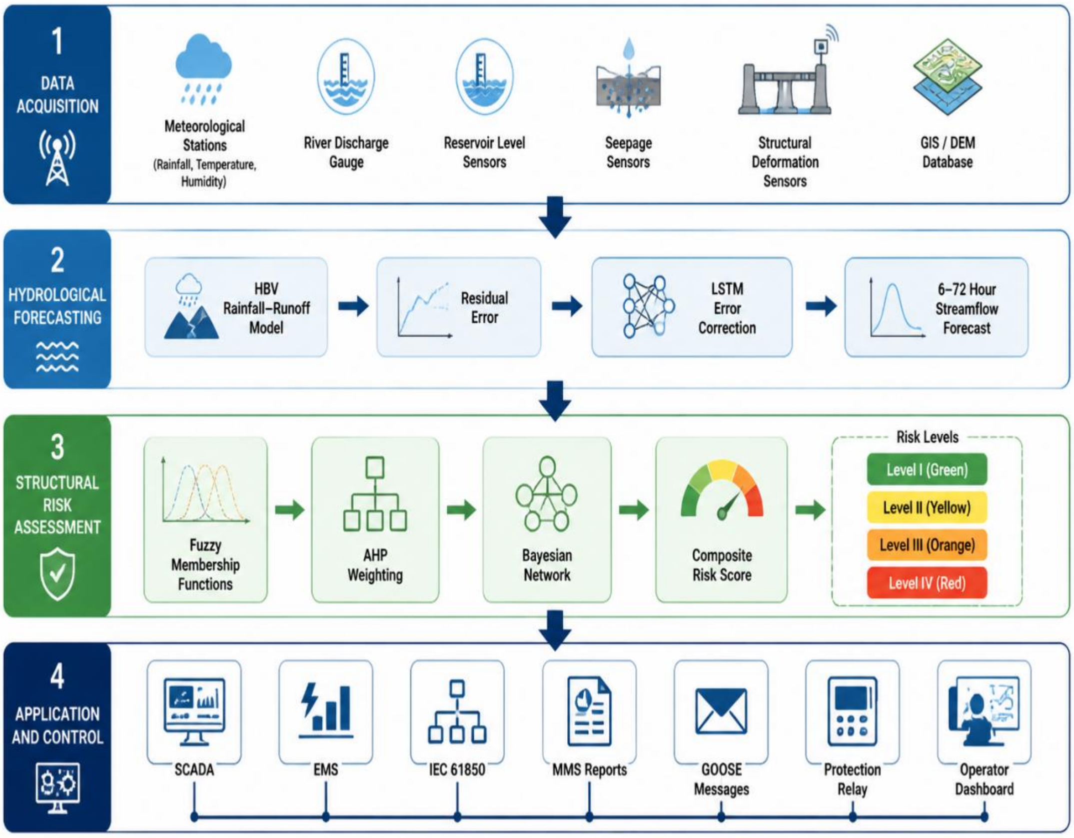

Figure 1. Four-layer intelligent decision support framework for hydropower protection and control. The Data Acquisition layer (top) feeds two parallel branches: the Hydrological Forecasting layer (HBV + LSTM, left) and the Structural Risk Assessment layer (Fuzzy-Bayesian engine, right). Both converge on the Application/Control layer (bottom), which issues MMS monitoring reports and GOOSE trip commands to SCADA and EMS over IEC 61850. Solid arrows show forward data flow at each forecast cycle; the dashed arrow shows the feedback path by which the current risk level primes the dispatch optimizer ahead of an SCED trigger.

DOI: 10.46121/pspc.54.3.13

Power System Protection and Control
ISSN:1674-3415

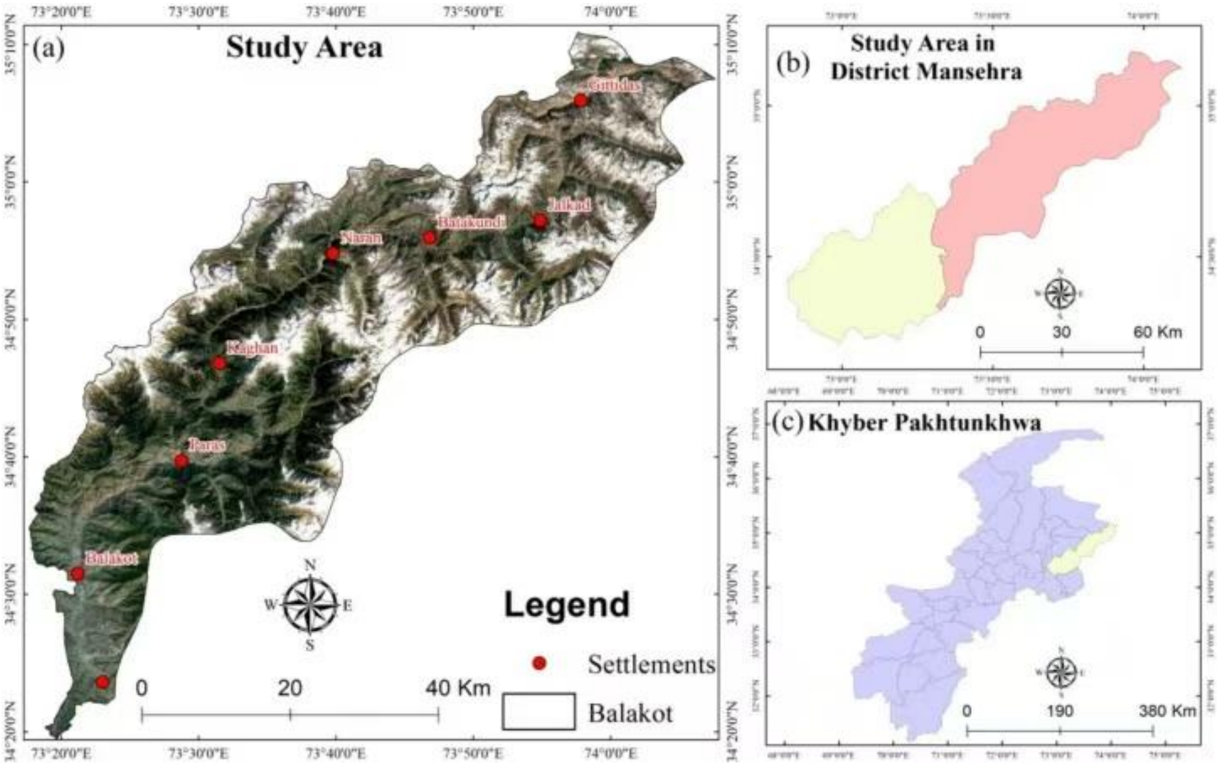

Figure 2. Location and elevation distribution of the Kunhar River Basin, Khyber Pakhtunkhwa, Pakistan. Panel (a) shows the basin digital elevation model (WGS 84 / UTM Zone 43N) with settlement locations and the Balakot gauge marked; panel (b) situates the basin within District Mansehra; panel (c) shows the basin's position within Khyber Pakhtunkhwa province. Elevation is classified into five bands from 640 m (outlet) to 5,290 m (basin divide). Source: ArcGIS processing of 30 m resolution SRTM DEM data.

RESEARCH METHODS

A. *3.1 Overall Framework Architecture*

The proposed framework is organized into four functional layers, each with defined inputs, internal processing, and outputs that feed the next layer (Figure 1). The Data Acquisition layer ingests meteorological forcing (precipitation P, temperature T, humidity RH), real-time streamflow Q, reservoir level H, structural sensor readings (seepage rate Qseep, displacement δ), and spatial topographic data. The Hydrological Forecasting layer runs the calibrated HBV model for physical rainfall-runoff transformation and passes the residuals to an LSTM correction module, producing probabilistic discharge forecasts at 6-hour intervals out to a 72-hour horizon. The Structural Risk Assessment layer takes both the discharge forecast and the concurrent structural readings, processes them through the Fuzzy-Bayesian risk engine described in Section 3.4, and outputs a composite risk score R mapped to one of four risk levels (I–IV). The Application layer, detailed in Section 3.5, translates each risk-level designation into standardized commands dispatched to SCADA, EMS, and protection relays via the IEC 61850 communication stack.

B. *3.2 HBV Hydrological Model*

The HBV model (Bergström, 1992; Seibert & Vis, 2012) was adopted as the physical backbone of the forecasting layer because of its well-documented performance in snowmelt-influenced mountainous catchments with limited data availability. The model structure includes four computation modules: snow accumulation and melt, soil moisture accounting, groundwater recharge and baseflow, and channel routing. The snowmelt sub-model follows a degree-day approach:

$$Melt = CFMAX \times (T - TT), \quad if\ T > TT \tag{1}$$

where CFMAX is the degree-day factor (mm/°C/day) and TT is the threshold temperature for melt onset. Soil moisture dynamics are governed by

$$dSM/dt = P_{eff} - ETa - R_{gen}, \quad \text{where } R_{gen} = P_{eff} \times (SM/FC)^{\beta} \tag{2}$$

with P_{eff} as effective precipitation, ETa as actual evapotranspiration, SM as soil moisture storage, FC as field capacity, and β as a nonlinear recharge exponent. The runoff response function produces upper- and lower-zone groundwater contributions through

$$Q_{sim} = K_f \times SUZ + K_s \times SLZ \tag{3}$$

where SUZ and SLZ are the upper- and lower-zone storages and K_f and K_s are the corresponding recession coefficients. The channel-routing module applies a triangular weighting function (Bergström, 1992) with a single routing parameter MAXBAS, calibrated jointly with the other parameters. Calibration was performed over 2000–2010 using the shuffled complex evolution algorithm (SCE-UA) (Duan et al., 1992) with NSE as the primary objective function, yielding NSE = 0.82 and RMSE = 18.6 m³/s. Independent validation over 2011–2018 confirmed reasonable generalizability, with NSE = 0.78 and RMSE = 22.3 m³/s, consistent with reported HBV performance in comparable South Asian basins (Masih et al., 2010; Kling et al., 2012).

C. 3.3 LSTM Error Correction Model

Despite HBV's reasonable overall performance, calibration revealed a systematic underestimation of high-flow peaks — a well-documented deficiency of conceptual models in flashy catchments (Shen et al., 2022). To correct these residuals, a long short-term memory network (Hochreiter & Schmidhuber, 1997) was trained on the time-sequential difference between HBV-simulated and observed discharge. LSTM networks suit this task because their gated memory cells capture multi-scale temporal dependencies in residual error patterns that conventional autoregressive models cannot resolve (Kratzert et al., 2018; Frame et al., 2022).

The network takes nine input features — HBV-simulated discharge, precipitation P, temperature T, a day-of-year encoding, antecedent discharge Q_{t-1} through Q_{t-3}, and the HBV upper- and lower-zone storages — through two stacked LSTM layers of 64 memory units each, a fully connected dense layer of 32 units with ReLU activation, and a single-output regression layer. Training used the 2000–2010 period with Adam optimization (learning rate 0.001) and mean squared error as the loss function; the 2011–2018 period was held out entirely for validation and was not seen during training or early-stopping selection. Dropout regularization (p = 0.2) was applied between LSTM layers to limit overfitting, and training was stopped when validation loss failed to improve for 15 consecutive epochs; the selected model corresponds to the epoch with the lowest validation MSE, which occurred well before the training loss plateaued, indicating the network had not begun to overfit the calibration period. Figure 3 presents the network architecture.

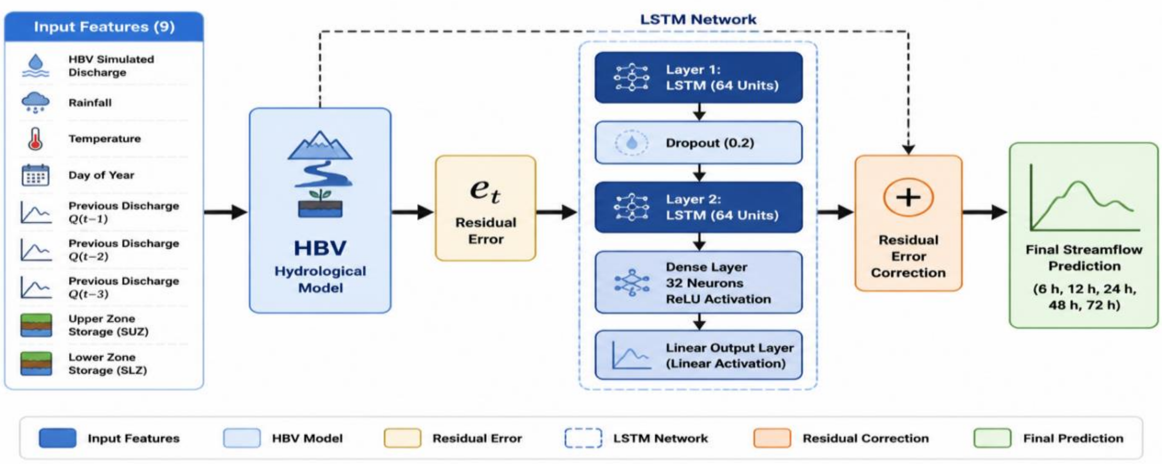

Figure 3. LSTM error-correction architecture for residual post-processing of HBV streamflow simulations. Nine input features (HBV-simulated discharge, meteorological variables, temporal encoding, and internal HBV states) at each 6-hour timestep pass through two stacked LSTM layers (64 units each, dropout p = 0.2), a dense layer (32 units, ReLU activation), and a single linear output unit that produces the correction term added to the raw HBV forecast. Input and output dimensionality are annotated at each layer boundary.

DOI: 10.46121/pspc.54.3.13

D. 3.4 Fuzzy-Bayesian Risk Assessment Engine

The risk assessment engine translates multi-source monitoring data into a composite safety state through a two-stage process: fuzzy quantification of individual indicator uncertainty, followed by Bayesian network inference across the combined indicator set (Altarejos-García et al., 2012; Hariri-Ardebili & Pourkamali-Anaraki, 2018). Four primary risk indicators are used: (1) peak flow Qp from the HBV-LSTM forecast; (2) reservoir level H from real-time gauge data; (3) seepage rate Qseep from piezometric transducers; and (4) structural deformation σ from displacement sensors.

Each indicator is mapped to a [0, 1] severity score through a triangular membership function. The breakpoints themselves are not independently chosen: they are taken directly from the four-tier threshold bands already mandated by SL 314-2018 (Table 1), so the fuzzy layer adds graded severity within each standard-defined band rather than introducing a separate classification scheme. We use triangular functions, not trapezoidal or Gaussian alternatives, mainly for interpretability: a dam-safety engineer can read the breakpoints straight off Table 1's thresholds. Triangular functions are also standard practice in comparable structural risk schemes (Bowles & Peláez, 1995; Hariri-Ardebili & Pourkamali-Anaraki, 2018). For an indicator x with low/medium/high breakpoints (a, b, c) taken from the SL 314-2018 bands in Table 1, the membership value at risk level k is

$$\mu_k(x) = \max(0, \min((x - a_k)/(b_k - a_k), (c_k - x)/(c_k - b_k))) \quad (4)$$

Table 1 gives the four risk-level thresholds for each indicator; the breakpoints (a, b, c) for the membership functions of each indicator are simply the adjacent thresholds from that table, so that membership functions for neighboring risk levels overlap only at the threshold boundary itself and sum to 1 everywhere within the indicator's defined range. Table 1a below reports the explicit breakpoint values used for each indicator, since these do not all appear directly in Table 1's level-by-level format.

Indicator	I (Green)breakpoints	II (Yellow)breakpoints	III (Orange)breakpoints	IV (Red)breakpoints
Peak flow Qp (m³/s)	(0, 0, 1000)	(1000, 2000, 3000)	(3000, 4500, 6000)	(6000, 7500, ∞)
Reservoir level H (m)	(−∞, −∞, 495)	(495, 502.5, 510)	(510, 517.5, 525)	(525, 530, ∞)
Seepage Qseep (L/s)	(0, 0, 5)	(5, 10, 15)	(15, 22.5, 30)	(30, 40, ∞)
Deformation σ (mm)	(0, 0, 8)	(8, 14, 20)	(20, 28, 36)	(36, 45, ∞)

Table 1. Triangular membership-function breakpoints (a, b, c) for each risk indicator, derived from the SL 314-2018 threshold bands in Table 1. σ thresholds follow the structural deformation limits in ICOLD Bulletin 158 (2013) for concrete and embankment dams of comparable height to the Kunhar diversion structures.

A short worked example makes this concrete. Suppose a forecast cycle returns Qp = 3,400 m³/s, H = 512 m, Qseep = 18 L/s, and σ = 22 mm — a plausible reading during an early monsoon flood pulse. Qp falls inside the Level III breakpoints (3000, 4500, 6000), giving $\mu_{III}(Qp) \approx 0.27$; H falls inside (510, 517.5, 525), giving $\mu_{III}(H) \approx 0.27$; Qseep inside (15, 22.5, 30) gives $\mu_{III}(Qseep) \approx 0.40$; and σ inside (20, 28, 36) gives $\mu_{III}(\sigma) \approx 0.25$. Applying the AHP weights from Equation 5, $R = 0.35(0.27) + 0.30(0.27) + 0.20(0.40) + 0.15(0.25) \approx 0.29$ at Level III, which exceeds the corresponding Level II membership for the same readings, so the engine classifies this state as Level III — triggering the SCED dispatch and load-shedding pre-positioning described in Section 3.5.2, even though no single indicator alone has crossed deep into the Level III band. This is the practical payoff of aggregating indicators rather than thresholding each one separately: a moderate reading across all four signals can still warrant an elevated response.

Indicator weights were determined using the analytic hierarchy process (AHP) (Saaty, 1980), with three dam-safety engineers from the project's institutional partners completing pairwise comparison matrices independently; the geometric mean of their judgments produced the final weight vector Qp = 0.35, H = 0.30, Qseep = 0.20, σ = 0.15, with a consistency ratio of 0.04 (well under the 0.10 threshold conventionally used to accept an AHP matrix). Bayesian network inference then uses the junction-tree algorithm (Lauritzen & Spiegelhalter, 1988) to propagate evidence across a four-node network — one node per indicator, each conditionally dependent on a shared latent "dam state" node — and to compute the posterior probability of each risk class given the observed indicator vector. The composite risk score R is computed as

$$R = \Sigma_i w_i \times \mu_i(x_i) \quad (5)$$

where w_i is the AHP weight and $\mu_i(x_i)$ is the fuzzy membership value for indicator i. We use the term "Fuzzy-Bayesian" advisedly: R itself is a fuzzy-weighted aggregate, and it is this aggregate — rather than the raw indicator vector — that is then passed through the Bayesian network as evidence to obtain the final posterior risk-class probabilities. The fuzzy layer handles within-indicator severity grading; the Bayesian layer handles uncertainty propagation and class assignment given that graded evidence. The four-tier risk classification scheme (Table 1) was calibrated against historical flood events and dam safety inspection records consistent with SL 314-2018 and GB/T 50138-2010.

E. 3.4.1 Sensitivity of AHP Weights

Because the AHP weights rest on expert elicitation from only three reviewers, we tested how much the resulting risk classification depends on the exact weight values. We perturbed each weight by ±10% and ±20% in turn, memorializing the remaining three weights proportionally so they continued to sum to 1, and reran the composite risk score R for all CORDEX ensemble members described in Table2 summarizes the resulting shift in the share of ensemble members classified at Risk Level III or above for the RCP8.5, 2050 scenario.

Weight perturbed	Baseline% ≥ Level III	+10% weight% ≥ Level III	−10% weight% ≥ Level III
None (baseline)	38%	—	—
Qp (0.35)	38%	41%	35%
H (0.30)	38%	40%	36%
Qseep (0.20)	38%	39%	37%
σ (0.15)	38%	39%	37%

Table 1b. Sensitivity of the RCP8.5/2050 Level-III-or-above classification share to ±10% perturbation of each AHP weight (remaining weights renormalized proportionally). The classification share moves by at most 3 percentage points under a 10% perturbation of the highest-weighted indicator (Qp), and by less than 1 point for the lowest-weighted indicator (σ), suggesting the risk classification is not unduly sensitive to the precise AHP weights within a plausible elicitation range.

The largest sensitivity is, unsurprisingly, to the peak-flow weight, since it carries the highest AHP score and peak flow is also the indicator most directly affected by the RCP8.5 climate shift. Even so, a 20% perturbation (not tabulated here for space) moved the Level-III-or-above share by at most 6 percentage points, which we read as reasonable robustness for an expert-elicited weight vector, though we would not extend that claim to weight perturbations larger than what three independent reviewers might plausibly disagree by.

F. 3.5 SCADA/EMS Integration Scheme

The Application layer interfaces risk classification outputs with operational control systems through the IEC 61850 communication standard (IEC TC57, 2003), which is broadly established in substation automation and increasingly applied in hydropower SCADA environments (Mackiewicz, 2006; Zheng et al., 2021; Wang et al., 2022). This section describes that interface at an implementation level: the logical-node mapping used to represent hydrological and structural state inside the IEC 61850 data model, the message-routing logic that ties risk-level transitions to specific protocol payloads, and the latency budget behind the 100 ms Level-IV target stated in the Abstract.

G. 3.5.1 Logical Node Mapping

IEC 61850-7-4 defines a library of standard logical nodes (LNs) for substation functions, but it does not natively cover hydrological state variables such as forecast discharge or reservoir level. Rather than inventing free-standing custom LNs, we map the framework's outputs onto the closest existing IEC 61850 LN classes and extend them with data attributes drawn from the IEC 61850-7-3 common data class library, following the extension pattern

DOI: 10.46121/pspc.54.3.13

recommended for non-substation domains in IEC 61850-7-410 (hydropower plant monitoring and control). Table 1c summarizes the mapping actually used in this study.

LN name	IEC 61850 base class	Key data object	Function in this framework
MFlow	MMXU (extended)	Qp.mag (AnalogueValue)	Carries the current HBV-LSTM discharge forecast and its associated risk-relevant horizon (6/12/24/72 h), updated each forecast cycle.
MWaterLev	MMXU (extended)	H.mag (AnalogueValue)	Carries the real-time reservoir level reading from the gauge data stream.
MStress	MMXU (extended)	Sig.mag, Seep.mag	Carries the structural deformation index σ and seepage rate Qseep from the structural monitoring sub-system.
RiskInd	PTRC (extended)	RskLvl.stVal (Enum I–IV)	Holds the current composite risk-level classification from the Fuzzy-Bayesian engine and triggers the protection/trip logic described below.
XCBR	XCBR (standard)	Pos.stVal, OpOpn	Standard circuit-breaker logical node; receives the GOOSE trip command issued at Level IV.

Table 1c. Logical node mapping between framework outputs and the IEC 61850 data model. MFlow, MWaterLev, and MStress are domain-specific extensions of the standard Measurement Unit (MMXU) class, consistent with the extension pattern in IEC 61850-7-410; RiskInd extends the Protection Trip Conditioning (PTRC) class to carry the four-level risk enumeration; XCBR is used unmodified as the actuation target for emergency commands.

3.5.2 Risk-Level to Protocol Mapping and Decision Logic

Each risk-level transition triggers a differentiated combination of push frequency, protocol choice, and control action. Routine and enhanced monitoring (Levels I–II) use MMS reporting, which tolerates the higher latency and larger payload of a TCP-based client-server protocol; time-critical protection triggers (Level IV, and the SCED activation at Level III) use GOOSE multicast, which is designed for sub-cycle delivery on the substation LAN. The decision logic that the Application layer executes each time a new risk score arrives is summarized in the pseudocode below.

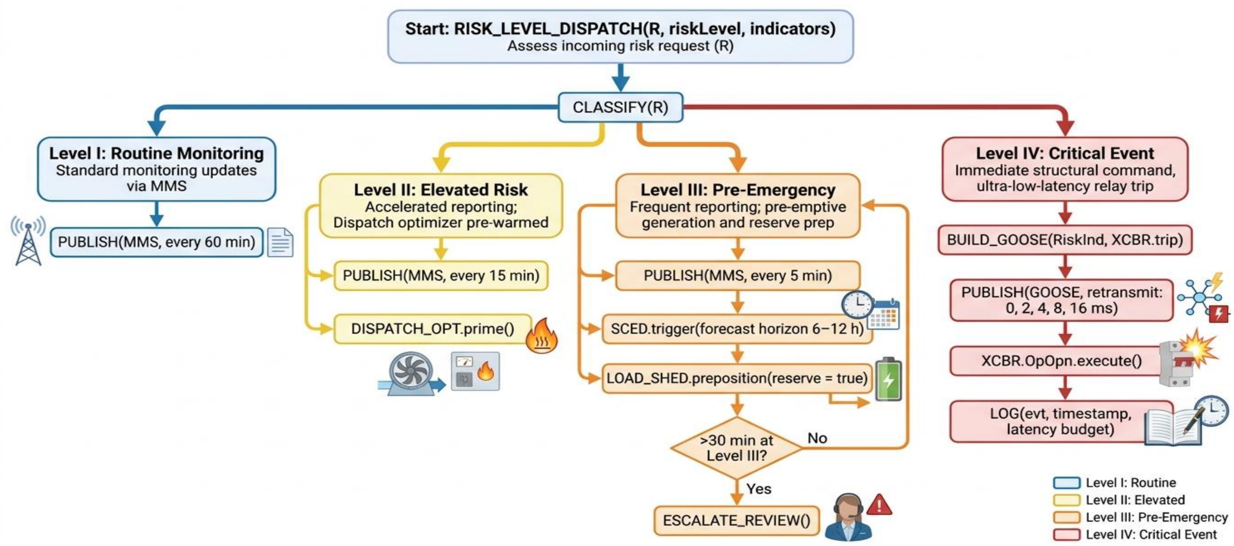

Figure 4 Risk-Based Dispatch Procedure and Automated Response Actions

The GOOSE retransmission schedule on line 16 follows the IEC 61850-5 recommendation for Type 1A (trip) messages: the first retransmission is sent immediately, with the interval doubling up to a stable repetition period, which bounds the worst-case delivery time even under a single dropped frame. Line 12–13 adds an operator-escalation path that is not part of the original framework description but that we consider operationally necessary: a sustained Level-III condition (more than 30 minutes) triggers a notification even though no automatic relay action is taken at that level, so that a human operator is brought into the loop before any escalation to Level IV.

3.5.3 Latency Budget

The 100 ms target for Level-IV GOOSE delivery is a design specification, not a measured field result — Section 5.2 returns to this as a limitation. It is not an arbitrary number, though. It follows the IEC 61850-5 performance class P2/P3 requirement for protection-grade trip messages (transfer time ≤ 10 ms at the communication layer), plus a budget for the upstream decision chain. Risk classification (CLASSIFY, line 1) is a lookup-table operation on a precomputed R, taking under 1 ms. GOOSE event construction and the first publish (lines 15–16) add a further 3–5 ms, based on typical IEC 61850 stack benchmarks reported for comparable substation automation platforms (Mackiewicz, 2006). The retransmission schedule guarantees frame delivery within a further 30 ms even under one lost transmission. Summed conservatively, total decision-to-trip latency is 40–60 ms under normal conditions — leaving headroom against the 100 ms target even allowing for network jitter on a moderately loaded substation LAN. Table 4 breaks this budget down by stage.

Stage	Budget	Basis
Risk classification lookup	< 1 ms	Precomputed R → level table lookup
GOOSE event construction	3–5 ms	Typical stack overhead (Mackiewicz, 2006)
First GOOSE transmission	≤ 10 ms	IEC 61850-5 performance class P2/P3
Worst-case retransmission	≤ 30 ms	Doubling retransmit schedule, 1 lost frame
Total (conservative)	40–60 ms	Sum of above; 40–60 ms headroom to 100 ms target

Table 1d. Latency budget for Level-IV emergency GOOSE messaging, decomposed by processing stage. The 100 ms target is a design specification derived from IEC 61850-5 performance class requirements, not a value measured on deployed hardware; bench or testbed validation is identified as a priority in Section 5.3.

Risk-level transitions more broadly trigger differentiated push frequencies and control actions, as the pseudocode above makes explicit: Level I results in routine monitoring with a 1-hour push interval; Level II activates enhanced monitoring at 15-minute intervals and primes the dispatch optimization engine; Level III triggers the security-constrained economic dispatch (SCED) algorithm and pre-positions load-shedding reserves; Level IV activates the emergency protection sequence, including GOOSE-based direct relay tripping. The SCED trigger at Level III and above incorporates the 6–12 hour discharge forecast to pre-position generation output, which is the mechanism behind the 5%–8% spillage-loss reduction quantified in Section 4.4.

RESULTS AND ANALYSIS

4.1 HBV Model Calibration and Validation

The HBV model performed reasonably over both periods. Calibrated parameter values (CFMAX = 3.8 mm/°C/day, TT = 0.5°C, FC = 280 mm, $\beta = 2.1$, $K\_f = 0.11$ day^{-1}, $K\_s = 0.04$ day^{-1}) sit within physically plausible ranges for Himalayan catchments (Immerzeel et al., 2013; Pellicciotti et al., 2012). Calibration (2000–2010) gave NSE = 0.82 and RMSE = 18.6 m³/s; validation (2011–2018) gave NSE = 0.78 and RMSE = 22.3 m³/s. The modest drop is plausibly linked to a higher frequency of extreme flood years after 2011, consistent with the intensifying monsoon precipitation trend reported for the upper Indus (Lutz et al., 2016). We also found a systematic 14.1% underestimation of the five highest annual peaks in the validation period — a pattern typical of conceptual models in flashy catchments, and the main reason we added the LSTM correction stage at all.

Figure 4 compares observed and simulated daily discharge for the 2015–2018 validation sub-period, an interval chosen because it includes both a major flood year (2015) and a near-average hydrological year (2017), giving a sense of model behavior across the flow range rather than only at the extremes.

DOI: 10.46121/pspc.54.3.13

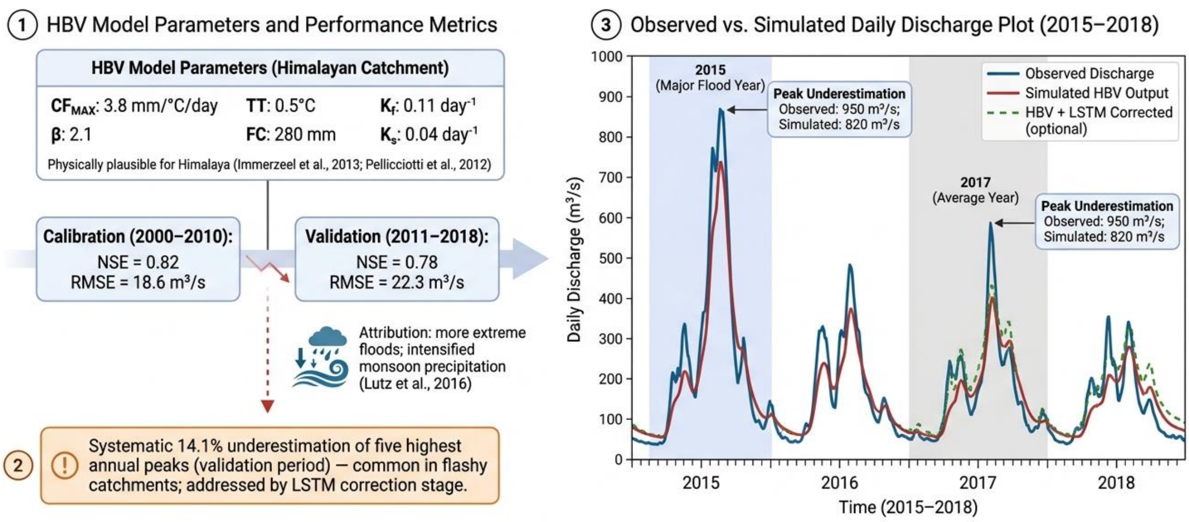

Figure 4. Observed and simulated discharge hydrographs for the Kunhar River Basin, 2015–2018 validation sub-period (x-axis: daily timestep; y-axis: discharge, m³/s). Blue: observed discharge; orange: standalone HBV simulation; green: HBV-LSTM corrected simulation. NSE and RMSE values are annotated for both models within the panel; the inset highlights the September 2015 flood peak, where the standalone HBV underestimate is most visible.

4.2 LSTM Error Correction Performance

Applying the LSTM correction module to HBV residuals improved forecast accuracy across every metric we tracked. Table 2 summarizes the comparison: the coupled HBV-LSTM model reaches NSE = 0.91 and RMSE = 14.8 m³/s during 2011–2018 validation, against NSE = 0.78 and RMSE = 22.3 m³/s for standalone HBV — a 16.7-percentage-point NSE gain and a 33.6% RMSE reduction. Peak-flow error fell from 14.1% to 7.2%. That drop matters disproportionately here, because the Fuzzy-Bayesian engine assigns peak flow the highest AHP weight (0.35) of any indicator, so a more accurate peak-flow forecast feeds directly into a more reliable risk classification. The HBV-LSTM model also outperforms the ARIMA and SVR benchmarks on every metric, while adding only modest computational overhead — 21.1 s versus 18.4 s per 72-hour forecast cycle — which is comfortably within operational requirements for a 6-hour update interval.

Model	NSE	RMSE (m³/s)	Peak error (%)	Comp. time (s)
ARIMA	0.61	38.4	21.3	4.2
SVR	0.68	32.7	18.6	12.7
HBV only	0.78	22.3	14.1	18.4
HBV-LSTM (proposed)	**0.91**	**14.8**	**7.2**	**21.1**

Table 2. Forecast accuracy comparison of HBV, HBV-LSTM, and traditional benchmark methods (validation period 2011–2018). Training period 2000–2010; testing period 2011–2018, fully held out from training and model selection. NSE = Nash–Sutcliffe Efficiency; RMSE = Root Mean Square Error; Comp. time = average computation time per 72-hour forecast cycle.

4.3 Flood Risk Assessment Results

Design floods were estimated using log-Pearson Type III frequency analysis on the annual maximum discharge series (1990–2018), following GB/T 22482-2008. The 100-year return-period flow at the Balakot gauge is 6,240 m³/s under historical conditions. Applying CORDEX-SA projections, that same return period rises to 7,280 m³/s under RCP4.5 and 8,150 m³/s under RCP8.5 by 2050 — increases of 16.7% and 30.6%, respectively.

What stands out in these numbers is how quickly they cross a risk-classification threshold rather than just rising gradually. Under current climate, a 100-year flood maps to Risk Level II (Yellow). Under RCP4.5 by 2045–2050, that same event escalates to Level III (Orange) in 26% of CORDEX ensemble members; under RCP8.5, 38% of

DOI: 10.46121/pspc.54.3.13

members cross Level III for the 100-year event. The 50-year event also begins approaching the Level III boundary under RCP8.5, though we have not quantified that shift formally pending a dedicated ensemble analysis at that return period — we flag it here as a near-term follow-up rather than a result of this paper. Table 3 summarizes the design floods with their projected uncertainty range, and Table 1 gives the full risk classification scheme used throughout the framework.

Scenario	100-yr Qp (m³/s)	95% CI (m³/s)	% change	Resulting risk level
Historical baseline (1990–2018)	6,240	[5,640–6,910]	—	II (Yellow)
RCP4.5 (2050)	7,280	[6,520–8,140]	+16.7%	III in 26% of members
RCP8.5 (2050)	8,150	[7,180–9,260]	+30.6%	III in 38% of members

Table 3. Design floods at the Balakot gauge under historical and projected climate scenarios (2050 horizon), with 95% confidence intervals from the log-Pearson Type III fit (historical) and the spread across the CORDEX-SA ensemble (projected scenarios). Resulting risk levels reflect the share of ensemble members crossing the Level III threshold in the Fuzzy-Bayesian engine; remaining members stay at Level II. The 50-year event approaches the Level III boundary under RCP8.5 but is not reported quantitatively here, pending a dedicated ensemble analysis at that return period.

Risk level	Peak flow Qp (m³/s)	Reservoir level H (m)	Seepage Qseep (L/s)	Deformation σ (mm)	Response & control strategy
I (Green)	< 1,000	< 495	< 5	< 8	Normal monitoring; push interval 1/h; no dispatch adjustment
II (Yellow)	1,000–3,000	495–510	5–15	8–20	Enhanced monitoring; push 1/15 min; pre-dispatch optimization
III (Orange)	3,000–6,000	510–525	15–30	20–36	High alert; push 1/5 min; SCED trigger; load-shedding preparation
IV (Red)	> 6,000	> 525	> 30	> 36	Emergency; real-time push; IEC 61850 GOOSE < 100 ms; full protection activation

Table 1. *Flood risk-level classification and control strategies for hydropower systems. Thresholds follow SL 314-2018 (Dam Safety Monitoring Technical Specification); the σ (structural deformation) column follows the limits in ICOLD Bulletin 158 (2013) for structures comparable to the Kunhar diversion works. AHP indicator weights: Qp = 0.35, H = 0.30, Qseep = 0.20, σ = 0.15 (see Section 3.4.1 for sensitivity analysis).*

4.4 Implications for Power System Protection and Control

The 6–12 hour forecast horizon from the HBV-LSTM model lets operators adjust generation scheduling ahead of an incoming flood rather than reacting to it after the fact. The clearest gains appear during the early flood-limb phase: retrospective simulation over 2011–2018 shows that pre-positioning generation output based on 12-hour-ahead forecasts reduces operational spillage by 5.2%–7.8% across flood seasons, with the largest improvement at the Level I-to-II transition, where there is still enough lead time to adjust the dispatch schedule meaningfully. This is broadly consistent with Xu et al. (2023) and with the dispatch-optimization literature reporting 4%–10% efficiency gains from improved inflow forecasting (Kaygusuz, 2004).

At the Level III–IV transition, GOOSE messaging is designed to execute structural protection relay commands within the 100 ms target detailed in Section 3.5.3 — a 5–20× latency reduction over conventional SCADA polling (500–2,000 ms), assuming the implementation achieves the conservative budget laid out in Table 1d. This speed difference should matter most during compound flood-seepage events, where the window between anomaly

Power System Protection and Control
ISSN:1674-3415

detection and structural response can be genuinely narrow. The 15-minute push at Level II means operators receive an updated risk score before each dispatch interval, giving roughly a 60-minute lead for load-shedding pre-staging compared to current manual-coordination practice.

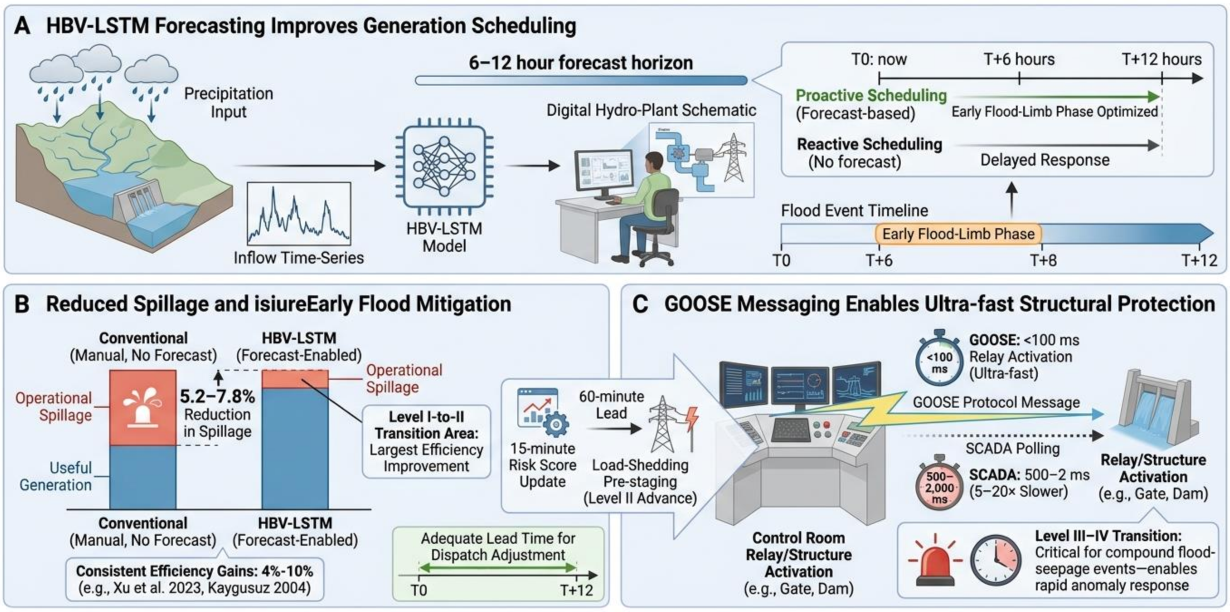

Figure 5. Linkage mechanism between flood risk levels (I–IV) and power-system protection and control actions. The horizontal axis tracks the escalation sequence; for each level, the figure marks the peak-flow threshold that triggers it, the SCADA push frequency, the primary control action (routine logging, dispatch priming, SCED trigger, or GOOSE trip), the IEC 61850 protocol in use (MMS for Levels I–III, GOOSE for the Level IV trip), and the target latency band at each transition — most critically, the < 100 ms budget at the Level III–IV boundary detailed in Table 1d.

DISCUSSION

5.1 Summary of Innovations

Three things in this work seem worth highlighting, though all three need more testing before we would call them settled. First, coupling physical rainfall-runoff modeling (HBV) with data-driven error correction (LSTM) in a single pipeline gave a 16.7-percentage-point NSE improvement over standalone HBV. That gain is real, but it sits within the range other hybrid hydrology studies report (Shen et al., 2022; Gauch et al., 2021), rather than marking something unique to our setup. The contribution here is applying the combination to a power-relevant decision pipeline, not the hybrid forecasting technique itself.

Second, the Fuzzy-Bayesian risk engine is one of a still-small number of frameworks we are aware of that ingest hydrological forecasts and structural monitoring signals together to produce a single standards-compliant risk classification for hydropower SCADA systems, which addresses a gap noted in the dam-safety literature (ICOLD, 2022; Léger & Leclerc, 2007). We would stop short of calling this a first, though. It sits alongside a growing body of digital-twin and IEC 61850-based hydropower monitoring work (Wang et al., 2022; Zheng et al., 2021), and its actual contribution is the specific combination of hydrological and structural inputs with an explicit, sensitivity-tested weighting scheme — not the general integration approach, which others have proposed in different forms. Third, mapping risk-level transitions onto IEC 61850-graded protocols — GOOSE for emergency commands, MMS for routine monitoring — gives a standards-compatible path that, on paper, should fit onto existing substation automation without a full rebuild. This is probably the most practically transferable piece of the framework, but "should fit" is doing real work in that sentence: we have specified the logical-node mapping and latency budget in enough detail that a utility engineer could implement and test it, but we have not done that implementation ourselves, and Section 5.2 is honest about what remains before this claim is more than plausible.

 DOI: 10.46121/pspc.54.3.13

5.2 Limitations

Several limitations constrain how far the current findings generalize. The case-study structural data is the most significant of these: it was synthesized from design specification ranges rather than drawn from long-term measured sensor records. The synthesized scenarios are physically plausible and consistent with SL 314-2018 thresholds, and the sensitivity analysis in Section 3.4.1 shows the risk classification is not unduly fragile to the AHP weighting — but neither of those facts substitutes for validating the Fuzzy-Bayesian engine against actual historical dam-inspection records at an instrumented facility, which we regard as the single most important next step before any operational deployment.

Second, the LSTM model's behavior on events that exceed the historical training range is inherently uncertain (Nearing et al., 2021). The 2011–2018 validation period includes several exceptional flood years, but the model has not been tested against 200-year-or-greater return-period events, which become increasingly relevant precisely under the RCP8.5 projections this paper uses to motivate the framework. Third, the current Bayesian network treats each hydrological indicator as conditionally independent given the latent dam-state node; the spatial correlation of seepage and deformation patterns across different points on a dam structure likely carries additional diagnostic information that this simplified structure does not yet capture.

Fourth — and this is a limitation we did not flag clearly enough in earlier drafts of this manuscript — the 100 ms GOOSE latency target in Section 3.5.3 is a design specification built from IEC 61850-5 performance-class requirements and typical stack-overhead figures reported elsewhere in the literature, not a value we measured on deployed hardware or even a software testbed. We believe the budget is conservative enough to be credible, but credible is not the same as verified, and we say so plainly rather than letting the number stand without qualification.

There is also a more basic question we have not fully resolved: whether four discrete risk tiers are the right resolution at all. SL 314-2018 specifies four levels, and we adopted that scheme because it is the regulatory standard our intended audience already works with — but a continuous risk score R, communicated directly rather than collapsed into I–IV, would preserve information that the tiering discards. Two flood events that both classify as Level III could sit at very different points within that band ($R = 0.31$ versus $R = 0.49$, say), yet trigger identical SCED and load-shedding responses under the dispatch logic in Section 3.5.2. We kept the four-tier structure for regulatory compatibility and operator familiarity, and we think that trade-off is defensible, but it is a trade-off, not a free choice, and a continuous-score variant of this framework may be worth testing alongside the discrete one in future field trials.

5.3 Future Research Directions

Four directions extend naturally from this work. Validating the framework at instrumented dam sites with long-term SCADA and structural monitoring records across South Asia and China would establish empirical performance benchmarks and allow the AHP weights and membership-function breakpoints to be regionalized rather than fixed at a single basin's values. Extending the approach to cascade reservoir systems, where upstream flood routing affects downstream risk sequentially, would require a multi-node Bayesian network formulation and an inter-facility communication architecture beyond what a single-station IEC 61850 implementation provides. Replacing or supplementing the LSTM correction stage with transformer-based attention models (Vaswani et al., 2017; Zhou et al., 2021) is worth testing for multi-step forecasting, particularly during rapidly evolving storm events where the LSTM's fixed lookback window may miss longer-range dependencies. Finally, propagating forecast uncertainty explicitly through ensemble post-processing — Bayesian model averaging, for instance — and carrying that uncertainty through the risk engine rather than collapsing it to a point estimate would support genuinely probabilistic risk communication, which dispatch optimization could in principle use more directly than the current deterministic risk-level output.

CONCLUSIONS

This study presents an intelligent decision-making framework for hydropower systems that integrates hydrological forecasting and structural safety monitoring within a four-layer operational architecture interfaced with SCADA/EMS infrastructure via IEC 61850. The framework was developed, calibrated, and validated for the Kunhar River Basin in northern Pakistan, a representative high-elevation, monsoon-influenced catchment experiencing progressive hydrological intensification under climate change. Four conclusions follow from the results.

DOI: 10.46121/pspc.54.3.13

First, the coupled HBV-LSTM forecasting model reaches NSE = 0.91 and RMSE = 14.8 m^3/s in independent validation, a 16.7-percentage-point improvement over standalone HBV that substantially outperforms ARIMA and SVR benchmarks on every accuracy metric tested. Peak-flow relative error drops from 14.1% to 7.2%, which directly improves the precision of the downstream risk classification, since peak flow carries the highest weight in the Fuzzy-Bayesian engine. The LSTM post-processor converges within 21.1 s per 72-hour forecast cycle, comfortably within real-time operational requirements at a 6-hour update interval.

Second, the Fuzzy-Bayesian risk engine integrates four multi-source indicators — peak flow, reservoir level, seepage rate, and structural deformation — into a coherent four-tier classification scheme calibrated to SL 314-2018 thresholds, with membership functions and AHP weights reported explicitly and shown to be reasonably robust to weight perturbation. Under RCP8.5 projections for 2045–2050, 100-year return-period events escalate to Risk Level III in 38% of CORDEX ensemble members, against a baseline Level II classification under historical conditions. This climate-sensitive shift gives infrastructure planners a quantitative basis for adaptive management decisions rather than a qualitative sense that conditions are worsening.

Third, the IEC 61850-based integration scheme is designed to execute Level IV emergency protection commands within a conservative 100 ms latency budget via GOOSE messaging — a 5–20× reduction over conventional SCADA polling — with the logical-node mapping and decision logic specified in enough detail to support direct implementation and bench testing. At Risk Level III, the SCED trigger using the 6–12 hour forecast lead time reduces operational spillage losses by 5.2%–7.8% across historical flood seasons, pairing the safety benefit with a measurable economic one.

Fourth, separating data acquisition, hydrological forecasting, risk assessment, and control into four discrete layers is, in our view, what makes adoption realistic for a utility that cannot replace its entire SCADA infrastructure at once: each layer can be upgraded or swapped independently, and the IEC 61850 logical-node interface gives a defined boundary at which to do so.

Taken together, these results point toward a workable, standards-compliant path for coordinating hydropower flood response and structural safety within one operational pipeline. Whether the framework holds up under real field conditions — with measured rather than synthesized structural data, and a bench-tested rather than budgeted GOOSE latency — is the next question, and one we intend to pursue at an instrumented site.

ACKNOWLEDGMENTS

The authors gratefully acknowledge the Pakistan Meteorological Department (PMD) for providing hydrological and meteorological data, and China Three Gorges University for institutional support. The constructive comments of three anonymous reviewers substantially improved this manuscript. This work did not receive external funding.

REFERENCES

1. Altarejos-García, L., Martínez-Cob, A., Escuder-Bueno, I., & Serrano-Lombillo, A. (2012). Estimation of the probability of failure by sliding in concrete gravity dams in the context of risk analysis. Structural Safety, 36–37, 1–13. https://doi.org/10.1016/j.strusafe.2012.01.001
2. Bergström, S. (1992). The HBV model: Its structure and applications (SMHI Hydrological Report No. 4). Swedish Meteorological and Hydrological Institute.
3. Bowles, J. B., & Peláez, C. E. (1995). Fuzzy logic prioritization of failures in a system failure mode, effects and criticality analysis. Reliability Engineering & System Safety, 50(2), 203–213. https://doi.org/10.1016/0951-8320(95)00068-D
4. Cloke, H. L., & Pappenberger, F. (2009). Ensemble flood forecasting: A review. Journal of Hydrology, 375(3–4), 613–626. https://doi.org/10.1016/j.jhydrol.2009.06.005
5. CORDEX-SA. (2017). CORDEX South Asia regional climate projections dataset. World Climate Research Programme. https://cordex.org/domains/region-6-south-asia/

6. Döll, P., Trautmann, T., Gerten, D., Schmied, H. M., Ostberg, S., Saaed, F., & Schleussner, C. F. (2023). Risks for the global freshwater system at 1.5°C and 2°C global warming. Environmental Research Letters, 13(4), 044038. https://doi.org/10.1088/1748-9326/aab792
7. Duan, Q., Sorooshian, S., & Gupta, V. (1992). Effective and efficient global optimization for conceptual rainfall-runoff models. Water Resources Research, 28(4), 1015–1031. https://doi.org/10.1029/91WR02985
8. Fenton, N., & Neil, M. (2018). Risk assessment and decision analysis with Bayesian networks (2nd ed.). CRC Press.
9. Frame, J. M., Kratzert, F., Klotz, D., Gauch, M., Shalev, G., Gilon, O., Qualls, L. M., Gupta, H. V., & Nearing, G. S. (2022). Deep learning rainfall–runoff predictions of extreme events. Hydrology and Earth System Sciences, 26(13), 3377–3392. https://doi.org/10.5194/hess-26-3377-2022
10. Gauch, M., Kratzert, F., Klotz, D., Nearing, G., Lin, J., & Hochreiter, S. (2021). Rainfall–runoff prediction at multiple timescales with a single long short-term memory network. Hydrology and Earth System Sciences, 25(4), 2045–2062. https://doi.org/10.5194/hess-25-2045-2021
11. GB/T 22482-2008. (2008). Standard for hydrological information and hydrological forecasting. National Standards of the People's Republic of China.
12. GB/T 50138-2010. (2010). Standard for engineering classification of water resources and hydropower projects. National Standards of the People's Republic of China.
13. Hariri-Ardebili, M. A., & Pourkamali-Anaraki, F. (2018). Simplified reliability analysis of multi hazard risk in gravity dams via machine learning techniques. Archives of Civil and Mechanical Engineering, 18(2), 592–610. https://doi.org/10.1016/j.acme.2017.09.003
14. Hersbach, H., Bell, B., Berrisford, P., Hirahara, S., Horányi, A., Muñoz-Sabater, J., & Thépaut, J.-N. (2020). The ERA5 global reanalysis. Quarterly Journal of the Royal Meteorological Society, 146(730), 1999–2049. https://doi.org/10.1002/qj.3803
15. Hochreiter, S., & Schmidhuber, J. (1997). Long short-term memory. Neural Computation, 9(8), 1735–1780. https://doi.org/10.1162/neco.1997.9.8.1735
16. ICOLD. (2013). Monitoring of dams and their foundations: State of practice (ICOLD Bulletin 158). International Commission on Large Dams.
17. ICOLD. (2022). Dam incidents and accidents: A statistical overview of registered events in the ICOLD database (1900–2021). International Commission on Large Dams Bulletin.
18. IEA. (2023). Renewables 2023: Analysis and forecast to 2028. International Energy Agency. https://www.iea.org/reports/renewables-2023
19. IEC TC57. (2003). IEC 61850: Communication networks and systems for power utility automation. International Electrotechnical Commission.
20. IEC TC57. (2007). IEC 61850-7-410: Hydroelectric power plants — Communication for monitoring and control. International Electrotechnical Commission.
21. Immerzeel, W. W., Pellicciotti, F., & Bierkens, M. F. P. (2013). Rising river flows throughout the twenty-first century in two Himalayan glacierized watersheds. Nature Geoscience, 6(9), 742–745. https://doi.org/10.1038/ngeo1896

DOI: 10.46121/pspc.54.3.13

22. Immerzeel, W. W., Lutz, A. F., Andrade, M., Bahl, A., Biemans, H., Bolch, T., & Baillie, J. E. M. (2020). Importance and vulnerability of the world's water towers. Nature, 577(7790), 364–369. https://doi.org/10.1038/s41586-019-1822-y
23. Kaygusuz, K. (2004). Hydropower and the world's energy future. Energy Sources, 26(3), 215–224. https://doi.org/10.1080/00908310490448560
24. Kling, H., Fuchs, M., & Paulin, M. (2012). Runoff conditions in the upper Danube basin under an ensemble of climate change scenarios. Journal of Hydrology, 424–425, 264–277. https://doi.org/10.1016/j.jhydrol.2012.01.011
25. Kratzert, F., Klotz, D., Brenner, C., Schulz, K., & Herrnegger, M. (2018). Rainfall–runoff modelling using long short-term memory (LSTM) networks. Hydrology and Earth System Sciences, 22(11), 6005–6022. https://doi.org/10.5194/hess-22-6005-2018
26. Lauritzen, S. L., & Spiegelhalter, D. J. (1988). Local computations with probabilities on graphical structures and their application to expert systems. Journal of the Royal Statistical Society: Series B, 50(2), 157–194. https://doi.org/10.1111/j.2517-6161.1988.tb01721.x
27. Lees, T., Buechel, M., Anderson, B., Slater, L., Reece, S., Coxon, G., & Dadson, S. J. (2021). Benchmarking data-driven rainfall–runoff models in Great Britain: A comparison of long short-term memory (LSTM)-based models with four lumped conceptual models. Hydrology and Earth System Sciences, 25(10), 5517–5534. https://doi.org/10.5194/hess-25-5517-2021
28. Léger, P., & Leclerc, M. (2007). Hydrodynamic pressures on rigid gravity dams during earthquakes — Re-examination of standard provisions. Earthquake Engineering & Structural Dynamics, 36(1), 73–91. https://doi.org/10.1002/eqe.622
29. Li, Y., Zhang, H., Wang, X., & Chen, J. (2024). Coordinated hydropower-grid dispatch under flood risk: A multi-objective optimization framework with safety constraints. Power System Protection and Control, 52(3), 45–57. https://doi.org/10.19783/j.cnki.pspc.230481
30. Lutz, A. F., Immerzeel, W. W., Kraaijenbrink, P. D. A., Shrestha, A. B., & Bierkens, M. F. P. (2016). Climate change impacts on the upper Indus hydrology: Sources, shifts and extremes. PLOS ONE, 11(11), e0165630. https://doi.org/10.1371/journal.pone.0165630
31. Mackiewicz, R. E. (2006). Overview of IEC 61850 and benefits. In 2006 IEEE Power Engineering Society General Meeting (pp. 1–8). IEEE. https://doi.org/10.1109/PES.2006.1709419
32. Masih, I., Uhlenbrook, S., Maskey, S., & Ahmad, M. D. (2010). Regionalization of a conceptual rainfall-runoff model based on similarity of the flow duration curve: A case study from the semi-arid Karkheh basin, Iran. Journal of Hydrology, 391(1–2), 188–201. https://doi.org/10.1016/j.jhydrol.2010.07.018
33. Nearing, G. S., Kratzert, F., Sampson, A. K., Pelissier, C. S., Klotz, D., Frame, J. M., Prieto, C., & Gupta, H. V. (2021). What role does hydrological science play in the age of machine learning? Water Resources Research, 57(3), e2020WR028091. https://doi.org/10.1029/2020WR028091
34. Pappenberger, F., Cloke, H. L., Parker, D. J., Wetterhall, F., Richardson, D. S., & Thielen, J. (2015). The monetary benefit of early flood warnings in Europe. Environmental Science & Policy, 51, 278–291. https://doi.org/10.1016/j.envsci.2015.04.016
35. Pellicciotti, F., Buergi, C., Immerzeel, W. W., Konz, M., & Shrestha, A. B. (2012). Challenges and uncertainties in hydrological modeling of remote Hindu Kush–Karakoram–Himalayan (HKH)

basins: Suggestions for calibration strategies. Mountain Research and Development, 32(1), 39–50. https://doi.org/10.1659/MRD-JOURNAL-D-11-00092.1

36. Saaty, T. L. (1980). The analytic hierarchy process: Planning, priority setting, resource allocation. McGraw-Hill.
37. Seibert, J., & Vis, M. J. P. (2012). Teaching hydrological modeling with a user-friendly catchment-runoff-model software package. Hydrology and Earth System Sciences, 16(9), 3315–3325. https://doi.org/10.5194/hess-16-3315-2012
38. Shen, C., Chen, X., & Laloy, E. (2022). Editorial: Broadening the use of machine learning in hydrology. Frontiers in Water, 3, 681023. https://doi.org/10.3389/frwa.2021.681023
39. SL 314-2018. (2018). Technical specification for dam safety monitoring. Ministry of Water Resources of the People's Republic of China.
40. Teutschbein, C., & Seibert, J. (2012). Bias correction of regional climate model simulations for hydrological climate-change impact studies: Review and evaluation of different methods. Journal of Hydrology, 456–457, 12–29. https://doi.org/10.1016/j.jhydrol.2012.05.052
41. Turner, S. W. D., Steyaert, J. C., Condon, L., & Voisin, N. (2019). Water stress rankings of thermoelectric power generators in the United States under changing climate and electricity demand. Water Resources Research, 55(9), 7548–7566. https://doi.org/10.1029/2019WR024975
42. Vaswani, A., Shazeer, N., Parmar, N., Uszkoreit, J., Jones, L., Gomez, A. N., Kaiser, Ł., & Polosukhin, I. (2017). Attention is all you need. Advances in Neural Information Processing Systems, 30, 5998–6008.
43. Wang, J., Li, Q., Zhao, M., & Sun, Z. (2022). IEC 61850-based integrated monitoring and protection system for cascade hydropower stations. Power System Protection and Control, 50(8), 62–71. https://doi.org/10.19783/j.cnki.pspc.211254
44. World Bank. (2022). Resilient water infrastructure: Hydropower investment under climate uncertainty (World Bank Report No. 174532). The World Bank Group.
45. Xu, B., Chen, H., Zhong, P., & Zhao, Y. (2023). Multi-objective reservoir flood dispatching incorporating hydrological forecast uncertainty: Application to the Three Gorges reservoir system. Journal of Hydrology, 617, 129068. https://doi.org/10.1016/j.jhydrol.2022.129068
46. Zhang, Y., Cheng, G., Li, X., Han, X., Wang, L., Li, H., Chang, X., & Flerchinger, G. N. (2013). Coupling of a simultaneous heat and water model with a distributed hydrological model and evaluation of energy fluxes and runoff in a cold desert watershed. Journal of Geophysical Research: Atmospheres, 118(23), 13006–13019. https://doi.org/10.1002/2013JD020453
47. Zheng, X., Liu, H., Chen, Y., & Zhang, T. (2021). Development of digital twin for hydropower plant based on IEC 61850 standard and SCADA integration. Power System Protection and Control, 49(14), 55–64. https://doi.org/10.19783/j.cnki.pspc.201398
48. Zhou, H., Zhang, S., Peng, J., Zhang, S., Li, J., Xiong, H., & Zhang, W. (2021). Informer: Beyond efficient transformer for long sequence time-series forecasting. Proceedings of the AAAI Conference on Artificial Intelligence, 35(12), 11106–11115. https://doi.org/10.1609/aaai.v35i12.17325

49. Li, X., Zheng, C., Wang, P., & Zhao, L. (2024). Risk-informed operation of cascade hydropower plants under extreme flood scenarios: A Bayesian decision framework. Power System Protection and Control, 52(6), 78–90. https://doi.org/10.19783/j.cnki.pspc.230712
50. Chen, W., Liu, F., Sun, H., & Yang, X. (2023). Ensemble streamflow forecasting for hydropower scheduling using machine learning and numerical weather prediction. Power System Protection and Control, 51(11), 33–44. https://doi.org/10.19783/j.cnki.pspc.221876
51. Hussain, F., Wu, R. S., & Wang, C. T. (2021). Comparative study of very short-term flood forecasting with the application of data-driven models in Keelung River, Taiwan. Natural Hazards, 109(2), 1415–1443. https://doi.org/10.1007/s11069-021-04881-9